PAPER

Check for updates

A ratiometric electrochemical probe for the quantification of apixaban in unprocessed plasma samples using carbon aerogel/BFO modified glassy carbon electrodes†

Payam Shahbazi-Derakhshi,[ab] Mohammad Abbasi, [b] Amirhossein Akbarzadeh,[c] Ahad Mokhtarzadeh,[d] Hamid Hosseinpour[e] and Jafar Soleymani [*a]

A novel electrochemical probe was established for the quantification of apixaban (APX) in unprocessed plasma samples. Efficiently oxidized graphene oxide aerogels (EEGO-AGs) and nano-sized $Bi_2Fe_4O_9$ (BFO) particles were electrodeposited on the surface of a glassy carbon electrode (GCE). In this work, a ratiometric electrochemical method was introduced for APX detection to enhance the specificity of the probe in plasma samples. The fabricated ratiometric probe was employed for the indirect detection determination of APX using $K_3[Fe(CN)_6]/K_4[Fe(CN)_6]$ as the redox pair. The differential pulse voltammetry technique was used to record the current alteration of the BFO/EEGO-AG-functionalized GCE probe at various APX concentrations. The probe response was proportional to the APX concentrations from 10 ng mL^{-1} to 10 µg mL^{-1} with a low limit of quantification (LLOQ) of 10 ng mL^{-1}. After validation, this method was successfully utilized for the determination of APX in patients' plasma samples who have taken APX regularly. The fabricated chemosensor detected APX concentrations in unprocessed plasma samples with high selectivity, resulting from the physical filtering antifouling activity of aerogels.

1. Introduction

Apixaban (APX) is a molecule with a molecular formula of $C_{25}H_{25}N_5O_4$ and a molecular weight of 459.5 g mol^{-1} and is known as a selective inhibitor of factor Xa.[1] Factor Xa is the final enzyme in the coagulation cascade and is responsible for the formation of fibrin clot by converting prothrombin to thrombin.[2,3] APX has no direct effect on platelet aggregation but indirectly reduces thrombin-induced clot formation by inhibiting the factor Xa.[1] By inhibiting the factor Xa, APX inhibits thrombin generation and thrombus development, showing an antithrombotic effect in the prevention of arterial and venous thrombosis at doses that maintain hemostasis.[4] The uses of APX in the treatment of acute venous thromboembolism include the prevention of stroke or systemic embolism in patients with

atrial fibrillation, after major orthopedic surgeries, *etc.*[5,6] APX possesses 50% bioavailability and is eliminated through multiple elimination routes, including renal excretion (25%) and hepatic metabolism (75%).[7,8] Anticoagulants are broadly employed in the prevention and therapy of thromboembolic diseases.[9] Direct oral anticoagulants (DOACs) are one of the popular therapies because of their predictable pharmacological influences and broader therapeutic concentration range.[10] One of the important advantages of DOACs such as APX is their targeted effect on a specific coagulation factor.[11] DOACs showed more desired pharmacokinetics than traditional coumarin-derived anticoagulants with low drug–drug and drug–food interactions.[12,13]

Currently, different guidelines are given for the dose adjustment of DOACs in specific populations involving hepatic and renal impairment, the elderly, and body weight.[10] However, a recent study found that about 25–50% of patients receive off-label doses, suggesting that DOAC overdose is associated with increased mortality and bleeding effects, whereas fewer DOACs with serious cardiovascular effects led to hospitalization.[14] Collectively, these facts highlight the significance of therapeutic drug monitoring (TDM) of DOACs, not only to assess patient adherence to therapy but also regulate their possible toxicity.[15] This requires the fabrication of reliable bioanalytical probes that can determine the plasma levels of DOACs and hence optimize drug therapy and control drug toxicity.[15,16]

*a*Pharmaceutical Analysis Research Center, Tabriz University of Medical Sciences, Tabriz, Iran. E-mail: jsoleymanii@gmail.com; soleymanij@tbzmed.ac.ir; Tel: +98 413 337 9323

*b*Liver and Gastrointestinal Research Center, Tabriz University of Medical Sciences, Tabriz, Iran

*c*Cardiovascular Research Center, Tabriz University of Medical Sciences, Tabriz, Iran

*d*Immunology Research Center, Tabriz University of Medical Sciences, Tabriz, Iran

*e*Department of Neurosurgery, Faculty of Medicine, Urmia University of Medical Sciences, Urmia, Iran

Conventional laboratory assays for DOACs are activated partial thromboplastin time (APTT) and prothrombin time (PT), which are not appropriate for reliable detection of DOACs.[17] Several representative analytical approaches have been reported in the literature for the determination of APX in real samples in the presence of its related impurities, which were mainly based on liquid chromatography.[18–20] However, these methods are originally laborious, time-consuming and need highly skilled persons to operate the instrument and interpret the obtained results. Electrochemical methods have some advantages of short analysis time, cost-effectiveness, high sensitivity, and the possibility to be a point-of-care testing method.

Electrochemical methods can convert the biological signals into electrical signals, respectively.[21–27] Due to the important progresses in nanotechnology, an increase in the electrochemical sensors is provided by the modification of the surface of electrodes. $Bi_2Fe_4O_9$ (BFO) is a semiconductor with high surface-to-volume ratio, making it a promising multifunctional material candidate for sensor designing uses.[28,29] Aerogels are three-dimensional (3D) and highly porous materials with ultralow density ($0.003\ g\ cm^{-3}$) and large specific surface area.[30] These specific features of aerogels led them to be employed in the fabrication of various devices. Electrochemical polymerization or electropolymerization is an electrode-surface modifying method in which a thin layer of polymer films is produced under an electrochemical condition using mostly potentiostatic (constant potential) or potentiodynamic (linearly scanned potential) techniques.[31–34]

In this study, a ratiometric electrochemical chemosensor was developed to detect APX in unprocessed plasma samples. To achieve this goal, a multilayer nanocomposite layer of efficiently oxidized graphene oxide aerogels (EEGO-AGs) and BFO were initially synthesized and then immobilized on the surface of the working electrode by the electrodeposition method. BFO/EEGO-

AG increases the geometrical surface of the GCE and enhances the interaction between the electrode and analyte. The fabricated sensor displayed significant electrochemical performance towards APX. As a result, with various analytical features, it is possible to identify and detect APX in patients' samples.
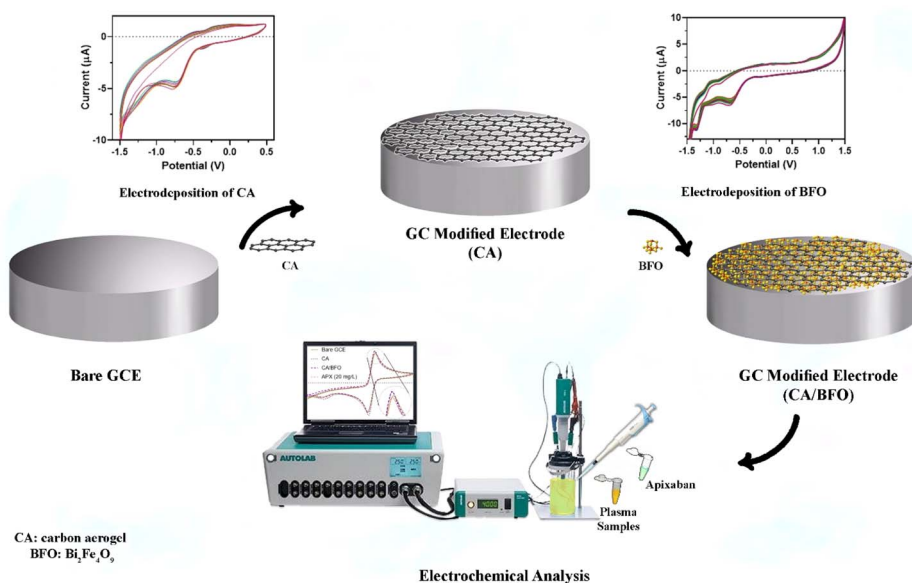
2. Experimental

2.1. Chemicals and reagents

APX was purchased from Exir pharmaceutical Co. (Karaj, Iran). Hydrochloric acid (HCl), sodium hydroxide, sulfuric acid (H_2SO_4), phosphoric acid (H_3PO_4), phosphorus pentoxide (P_2O_5), potassium permanganate ($KMnO_4$), graphite, sodium nitrate ($NaNO_3$), hydrogen peroxide (H_2O_2), and ascorbic acid (AA) were purchased from Sigma (Germany). Phosphate buffer solutions were prepared using NaH_2PO_4 and Na_2HPO_4. Also, a stock solution of APX ($200\ \mu g\ mL^{-1}$) was prepared by dissolving APX in the buffer solution (50 mM, pH = 6.0). Also, efficiently oxidized graphene oxide (EEGO) aerogel microparticles and BFO nanoparticles were dispersed in water through sonication. Triple deionized water was utilized for the preparation of any solution. Plasma samples were provided by the Iranian Blood Transfusion Organization (Tabriz, Iran).

2.2. Apparatus and measurements

All electrochemical measurements were recorded using an AUTOLAB electrochemical system equipped with a three-electrode system of reference (Ag/AgCl electrode), working (GCE, $d = 2$ mm, Azar Electrode Company (Urmia, Iran)), and counter (platinum electrode) electrodes. A field emission scanning electron microscope (FESEM, FEG-SEM MIRA3 TESCAN (Brno, Czech Republic)) was used to show the morphology of the materials. Fourier transform infrared (FTIR, Bruker model

Scheme 1 Schematic representation of the sensor fabrication and detection of APX using the electrochemical method.

instrument (Billerica, Massachusetts, US)) was utilized to characterize the functional groups.

2.3. Synthesis

2.3.1. Synthesis of GO. About 3 g $KMnO_4$ was added to a mixture of H_2SO_4 (23 mL, 98%) and P_2O_5 (1 g) and stirred for at least 3 min. Then, 1 g of graphite (200 mesh) and 0.5 g of $NaNO_3$ were added to the mixture and agitated for 15 min. The mixture was heated at 35 °C under stirring conditions for at least 1 h. The temperature of the reaction was controlled by the addition of water in different steps. Afterward, the temperature of the mixture was raised to 85 °C and held for 15 min. After cooling to ambient temperature, H_2O_2 (30%) was added to extra oxidize the GO and convert it to EEGO microparticles. Finally, the as-produced EEGO was washed with HCl and deionized water to remove unreacted or excess substances. EEGO was dried in an oven at 60 °C and stored at room temperature.[35,36]

2.3.2. Synthesis of EEGO-AGs. Briefly, 0.2 g of EEGO and 0.6 g of AA were added to about 50 mL of deionized water and sonicated for about 30 min to produce a homogeneous dispersion of EEGO. Then, it was heated up to 40 °C and kept for at least 20 h to produce a hydrogel. Next, the prepared graphene hydrogel was frozen and dried to get EEGO-AGs. Then, many holes were prepared on the produced AGs. Next, 25 mL of EEGO and AA with a 1 : 3 ratio was supplemented into the holes and pores and then kept at 40 °C for another 20 h to create the second stage of EEGO gelation. Finally, the as-prepared EEGO-AGs were collected by the freeze-drying technique.[37]

2.3.3. Synthesis of BFO nanoparticles. About 1.21 g of $Bi(NO_3)_3$ $5H_2O$ and 2.02 g of $Fe(NO_3)_3$ $9H_2O$ (1 : 2 molar ratio) were added into 7.5 mL of HNO_3 (2.0 M) solution. To deposit Bi^{3+} and Fe^{3+} ions, about 25 mL of KOH (2.0 M) was supplemented to the solution dropwise. The brown solid was collected using a centrifuge (10.000 rpm, 10 min) and washed with deionized water three times. Afterward, 20 mL of NaOH (12 M) was added to the solid and stirred for about 1 h. The dispersed mixture was moved into a 50 mL Teflon liner autoclave and kept at 180 °C for 24 h. After finishing the hydrothermal treatment, the mixture was cooled down to room temperature. Finally, the brown precipitate was centrifuged and washed several times with water and ethanol and dried at a temperature of 80 °C for about 4 h.[38]

2.4. Sensor fabrication

2.4.1. Electrode cleaning. Firstly, the GCE was polished with high-meshed alumina powder, followed by washing with water and putting it into acetone for about 5 min and then washing with deionized water. Then, the electrode was placed in the mixture of H_2SO_4 (0.05 M) and HNO_3 (0.050 M) for about 5 min and then washed with deionized water. Next, the electrode was inserted in H_2SO_4 (0.1 M) and CV was run for 25 cycles at the potential between −1.2 and 1.2 V to achieve repetitive CVs.

2.4.2. Electrodeposition of EEGO-AGs. Firstly, the GCE was immersed in an EEGO-AG (500 mg L^{-1}) solution. Then, the CV technique was employed in the potential range from −1.5 to 0.5 V against the Ag/AgCl reference electrode with a total cycle

and scan rate of 10 and 100 mV s^{-1}, respectively. During this step, EEGO-AG particles are attached to the surface of the GCE. Fig. 1 exhibits the consecutive CVs of the electrodeposition of EEGO-AGs on the surface of a GCE.

2.4.3. Electrodeposition of BFO on the surface of EEGO-AGs/GCE. EEGO-AGs/GCE was immersed in BFO dispersion with a concentration of 500 mg L^{-1}. Then, the CV technique was utilized to electrodeposit BFO nanoparticles on the EEGO-AG/GCE surface in the potential range from −1.5 to 1.5 V at a scan rate of 100 mV s^{-1} for 10 cycles. Fig. 2 shows the electrodeposition process of BFO on the surface of EEGO-AGs/GCE (Scheme 1).
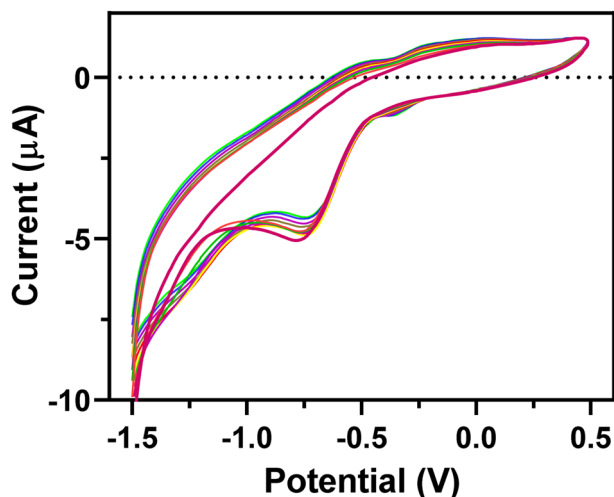

Fig. 1 The consecutive CVs of the electrodeposition of EEGO-AGs on the surface of a GCE (N = 10 cycles, scan rate = 100 mV s^{-1}, PBS = 50 mM, pH = 7.0).
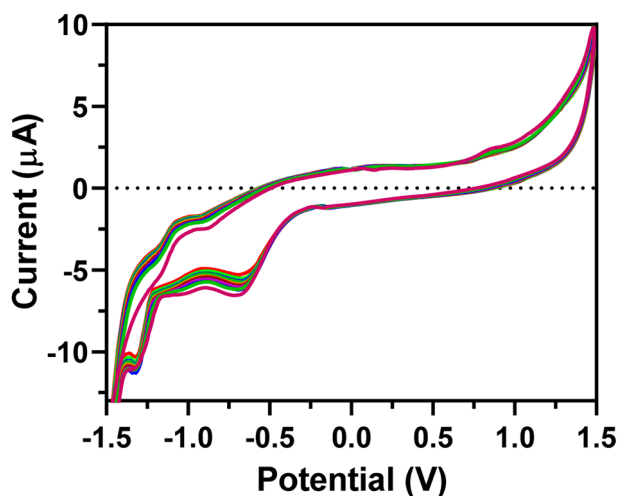

Fig. 2 The electrodeposition process of BFO NPs on the surface of the EEGO-AG-modified GCE (N = 10 cycles, scan rate 100 mV s^{-1}, PBS 50 mM, pH 7.0).

3.   Results and discussion

3.1.   Surface modification of the GCE with EEGO-AGs and BFO and characterization of nanoparticles

The EEGO-AG particles were electrodeposited onto the GCE through CV as explained in Section 2.4.2 and presented in Fig. 1. The increment of anodic peak current indicates the attachment of the EEGO-AGs and a growth in the amount of EEGO-AGs upon increasing the number of cycles. The surface of the electrodeposited EEGO-AG GCE electrode is irreversible and stable in the buffer solution. Upon electrodeposition of EEGO-AGs, the enhanced characteristic oxidation peak current at -0.5 V indicates efficient attachment of EEGO-AGs. The enhanced anodic peak current results from the further attachment of EEGO-AGs on the surface of the GCE. After 10-cycle scanning, the anodic peak remained constant, revealing the maximum attachment of GO on the electrode surface. The electrodeposited EEGO-AGs onto the GCE not only improve the electrocatalytic behavior but also enhance the active surface area for grafting BFO nanoparticles.

Upon modification of EEGO-AGs/GCE with BFO nanoparticles, the current of the BFO/EEGO-AG/GCE probe was further increased, which is mainly related to the electrocatalytic activity and high surface-to-volume ratio of BFO NPs (Fig. 2). Electrodeposition of BFO can regulate the electroanalytical properties of the EEGO-AGs/GCE by altering the morphology and available cavities. The anodic peak current is increased with increasing the cycle numbers and attachment of more BFO NPs onto the surface of the GCE, approving the improvement of electrocatalytic properties of the electrode. The optimum condition, *i.e.*, high anodic current is observed after 10 cycles, suggesting the lowest number of electrodeposition CVs for functionalization with BFO NPs.

The surface morphology of the BFO/EEGO-AG/GCE layer was investigated using FESEM. Fig. 3a reveals that that BFO/EEGO-AG is uniformly electrodeposited onto the GCE surface and displays rough and wrinkled-like sheets arisen by the GO structure. Indeed, this morphology of the deposited layer can facilitate the target analyte diffusion from the supporting electrolyte to the sensing layer near the surface of the GCE. Furthermore, the well-combined and well-dispersed BFO NPs with EEGO AGs may provide an enhanced surface area as a favourable substrate for the fabrication of highly sensitive electrochemical sensors.

Fig. 3b and c shows the FESEM images of the BFO NPs and EEGO AGs, respectively. Compared with the characteristic sheet-like morphology of EEGO, the BFO NPs exhibit a considerably diverse morphology. After electrodeposition of BFO NPs, the thin wrinkled EEGO sheets were totally covered by a layer of BFO NPs, which comprises different cavities to allow APX molecules to electrochemically react on the surface of the modified electrode.

Fig. S1a and b† shows the FTIR spectra of the EEGO AGs and $Bi_2Fe_4O_9$ particles, respectively. The GO has two chief absorption spectra at 1730 cm^{-1} and 1055 cm^{-1} corresponding to the C=O and C–O, respectively.[39] The hydrogen bond may be the main interaction to create the aerogel structure, which could be affected by the C=O and C–O position at the long wavenumber region (near 1740 cm^{-1}).[40] The absorption peak spectra at around 1420 cm^{-1} and 1610–1630 cm^{-1} range are attributed to
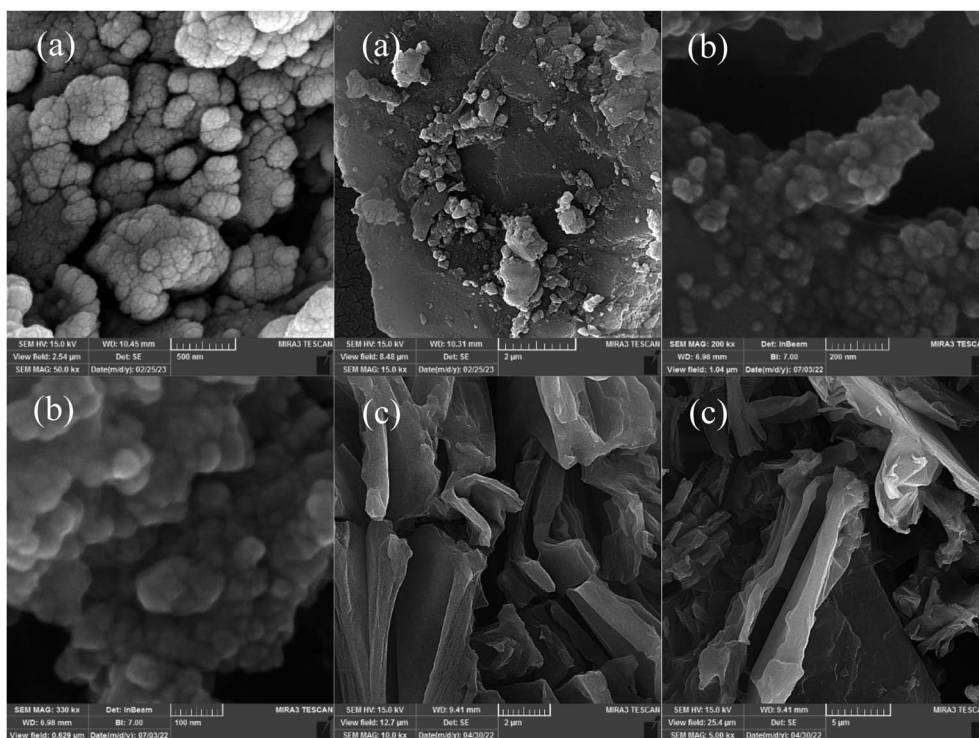

Fig. 3   SEM images of (a) surface of the BFO/EEGO-AG-modified GCE electrode, (b) BFO NPs, and (c) GO AGs on various scales.

the asymmetric carboxylic stretching vibration and the stretching vibration of C=C, respectively. The hydroxyl and carboxyl functional groups increase the integration between BFO and EEGO particles by a wide range of interactions.[41]

The stretching and bending vibrations of Fe–O are presented in the range of 400–813 cm^{-1}. BFO NPs have an orthorhombic structure with two different sites for four iron atoms, *i.e.*, octahedral and tetrahedral sites. The absorption peaks of octahedral and tetrahedral sites are present at 440 and 470 cm^{-1} (Fe cations in FeO_6), and 523 and 609 (O–Fe–O and Fe–O–Fe). The absorption peaks at 638 and 840 cm^{-1} correspond to the stretching vibration of the Fe ions in the FeO_4 tetrahedral structure. An absorption peak at 1636 cm^{-1} is devoted to the O–H stretching vibration of water.[42]

3.2. Electrochemical characterization of BFO/EEGO-AGs/GCE

Electrochemical performance of the redox probe was studied during step-by-step surface modification of the GCE using the CV technique, which offers important evidence of the BFO/EEGO-AG/GCE electrode performance in the presence and absence of APX. Fig. 4 illustrates the CVs of a bare GCE, EEGO-AGs/GCE, and BFO/EEGO-AGs/GCE in the presence and absence of APX (5 μg mL^{-1}) in the supporting electrolyte phosphate buffer solution (50 mM, pH = 6.0, 5 mM $Fe(CN)_6^{4-}$/$Fe(CN)_6^{3-}$) at the potential between −1.0 and +1.0 V with a scanning rate of 100 mV s^{-1}.

Upon modification of the surface of the bare GCE with EEGO-AGs and BFO particles, the electrochemical activity of the electrode is increased. The potential of the $Fe(CN)_6^{4-}$/$Fe(CN)_6^{3-}$ redox pair is altered from +0.31 to 0.29 V, approving the surface modification of the GCE with EEGO-AGs and BFO. The peak current at 0.29 V is decreased upon the addition of the analyte, which is a result of blocking of redox pair reduction and oxidation by APX. The nanoparticles enhance the specific surface area to facilitate the $Fe(CN)_6^{4-}$/$Fe(CN)_6^{3-}$ redox reaction.

3.3. Effect of pH

The electrochemical performance of the BFO/EEGO-AG/GCE probe is strongly influenced by the pH value. This effect on the peak potential and current of the redox pair was studied using the CV technique. Fig. 5a demonstrates the CVs at the pH from 2.0 to 10.0. Fig. 5b shows the E_{pa} *vs.* pH plots, and the following equation (eqn (1)) is obtained.

$$E_{pa} \text{ (V)} = 0.02171\text{pH} + 0.2079, \; R^2 = 0.9823 \qquad (1)$$

The obtained slope is 0.02171 V per pH, which is 2.5-fold lower than the theoretical value of 0.0592 V per pH, suggesting that in the presence of APX, in the electrochemical activity of the redox pair, the numbers of electrons and protons are not equal. Also, DPV results confirmed that the I_{pa} of BFO/EEGO-AGs/GCE was largely influenced by APX at pH = 4.0. Hence, pH = 4.0 was selected as the optimum pH value for recognition of APX in plasma samples.

Fig. 5 (a) CVs of BFO/EEGO-AGs/GCE at consecutive pH values from 2.0 to 10.0, and (b) E_{pa} *vs.* pH curve for the $Fe(CN)_6^{4-}$/$Fe(CN)_6^{3-}$ redox pair (PBS 50 mM, potential range from −1.0 to 1.0 V, scan rate 50 mV s^{-1}).
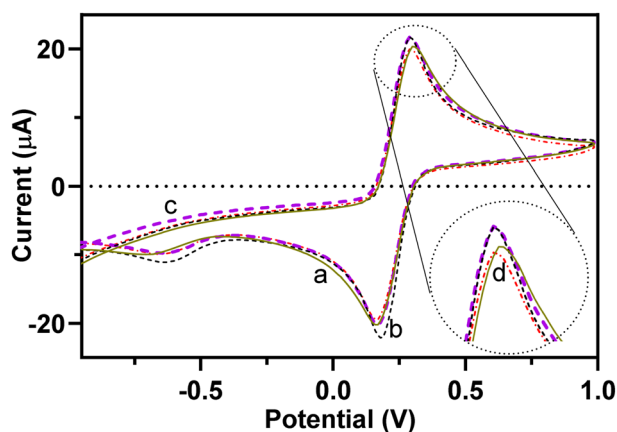

Fig. 4 (a) CVs of a bare GCE, (b) EEGO-AG modified GCE, and (c) EEGO-AG/BFO modified GCE in the absence and (d) presence of APX (20 mg L^{-1}) (PBS 50 mM, pH 4.0, scan rate 100 mV s^{-1}).

3.4. Kinetic study

The investigation of the influence of scan rate on the electrochemical reaction provides valuable information relating to the mechanism of mass transport and electron transfer. The mass transport mechanism in the electrochemical system could be controlled by adsorption and/or diffusion. Also, the electron transfer coefficient (α) and coverage of specific area (Γ^*) were calculated using the effect of scan rate. So, the kinetics of the BFO/EEGO-AG/GCE probe were evaluated in the presence of $Fe(CN)_6^{4-}/Fe(CN)_6^{3-}$ by plotting CVs at various scan rates ranging from 5 to 1000 mV s^{-1} (Fig. S2a†). The oxidation peak of $Fe(CN)_6^{4-}/Fe(CN)_6^{3-}$ appeared at the potentials higher than around +0.29 V at the scan rates between 5 mV s^{-1} and 1000 mV s^{-1} (Fig. S2a†). As seen, upon increasing the scan rate, the peak current also increased and the diffusion layer thickness decreased.[43]

The increase in peak current is proportional to the scan rate (Fig. S2b†), the determination of the surface area for electron transfer of the BFO/EEGO-AGs/GCE and the supporting electrolyte. The mathematical form of I_{pa} vs. ν plot could be obtained as I_{pa} (μA) $= 140.4\nu + 10.19$ with R^2 of 0.9586.

From Fig. S2c,† it is obvious that there is a linear relationship between anodic peak potential and ln ν (V s^{-1}), which can confirm the irreversible nature of electrochemical reactions at the BFO/EEGO-AGs/GCE. The E_{pa} is changed to the positive potentials by enhancing scan rate. The equation of E_{pa} vs. ln ν is as follows: E_{pa} (V) $= 0.01965 \ln \nu$ (V s^{-1}) $+ 0.3366$ with R^2 of 0.9536. The correlation between E_{pa} and scan rate is expressed by the Laviron theory for irreversible electrochemical reactions as follows:

$$E_{Pa} = E_0' + \frac{RT}{\alpha nF}\ln\left(\frac{RTk^\circ}{\alpha nF}\right) + \frac{RT}{\alpha nF}\ln \nu \quad (2)$$

in which F and T denote the Faraday constant (96 493 C mol^{-1}) and temperature (K) and R and n describe the gas constant (8.314 J mol^{-1} K^{-1}) and the number of electron transfer, respectively. E_0' is the formal potential, which could be calculated as $E_0' = \frac{E_{pa} + E_{pc}}{2}$. α and k° describe the coefficient of electron transfer and the reaction standard rate constant, respectively.

The mechanism of the redox process on the BFO/EEGO-AGs/GCE was checked using I_{pa} vs. ln ν and I_{pa} vs. $\nu^{0.5}$ (Fig. S2b and d†). The obtained findings proposed that the I_{pa} vs. $\nu^{0.5}$ has a linear trend with an intercept around zero in low scan rates, proposing the diffusion-controlled mechanism of the electrooxidation process. Also, the diffusion mechanism was further confirmed by the ln(I_{pa}) vs. ln(ν) plot with a general equation of ln(I_{pa}) $= 0.4494 \ln \nu + 4.323$ (R^2 of 0.9977) (Fig. S2e†). The slope of 0.4494 is close to 0.5, proposing the diffusion-controlled mechanism of the oxidation.

3.5. Analytical features of the developed probe

3.5.1. Linearity and sensitivity. BFO/EEGO AGs were employed as a versatile electrochemical probe for quantification of APX concentration in patients' plasma samples. In this study,

a layer-by-layer electrodeposition approach was used to precipitate BFO and EEGO AGs onto the bare GCE. Upon addition of EEGO AGs, the specific surface area was enhanced due to the high surface area-to-volume ratio of the composite, increasing the functionalization sites for the next step of surface modification. However, functionalization with EEGOs may result in low currents, which means reduced sensitivity. To address this issue, BFO nanoparticles are incorporated, and the metallic nature of these nanoparticles enhances the signal. The addition of EEGO AGs to the surface of the GCE not only enhances the specific surface area accessible to functionalize with BFO NPs but can provide an antifouling effect, raising the stability of the fabricated probe.[44]

The analytical feature of the EEGO AG/BFO modified GCE probe was determined using a [APX] vs. I_p plot and the DPV technique. Fig. 6a shows the DPV spectra of the EEGO AG/BFO modified GCE with increasing concentrations of APX in the plasma matrix. By increasing the APX level in plasma, the oxidation current of the redox pair is proportionally decreased. The deceased current displayed a wide linear range from 10 ng mL^{-1} to 10 μg mL^{-1} with a low limit of quantification (LLOQ) of
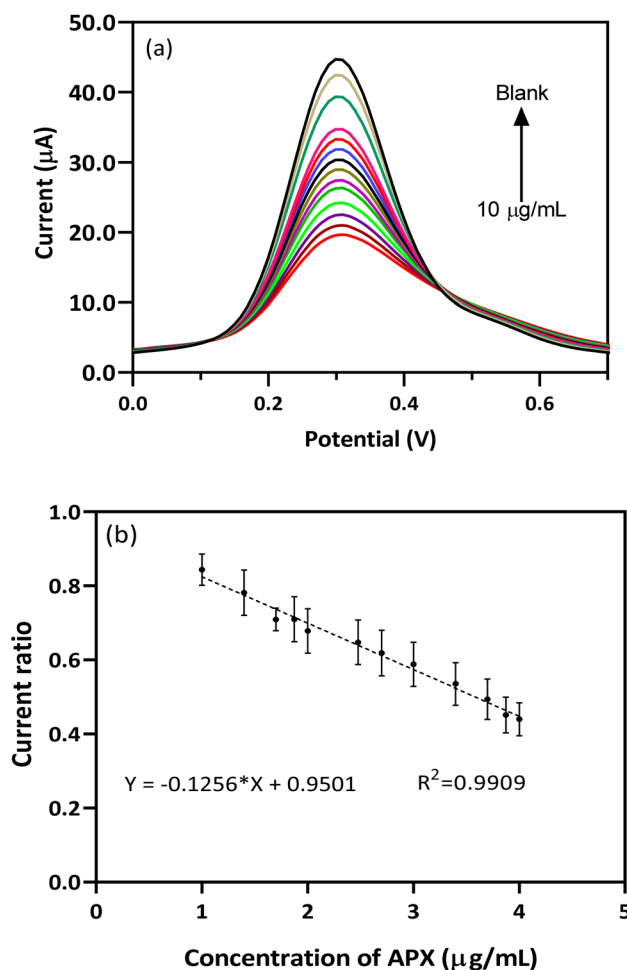

Fig. 6 (a) DPVs of BFO/EEGO-AGs/GCE in the presence of various concentrations of APX and (b) corresponding calibration curve in plasma samples (PBS 50 mM, scan rate 50 mV s^{-1}, pH = 4.0).

Table 1 Analytical techniques and performance of the developed methods for APX quantification

Technique	Dynamic range	LOD	LOQ	Ref.
LC/MS-MS	5–500 µg L^{-1}	2.0 µg L^{-1}	4.1 µg L^{-1}	48
UPLC-MS/MS	1.0–100 ng mL^{-1}	—	—	49
Electrochemical	1.99 µM–0.11 mM	0.68 µM	1.99 µM	50
HPLC-UV	—	—	8–39 ng mL^{-1}	51
HPLC	—	1.02 µg mL^{-1}	3.091 µg mL^{-1}	52
HPLC	—	0.05 g mL^{-1}	0.15 µg mL^{-1}	53
Spectrofluorometric	0.2–6 µg mL^{-1}	0.017 g mL^{-1}	0.057 µg mL^{-1}	54
LC-MS/MS	—	4 ng mL^{-1}	12 ng mL^{-1}	55
Electrochemical	10 ng mL^{-1} to 10 µg mL^{-1}	LLOQ: 10 ng mL^{-1}	Plasma	This work

10 ng mL^{-1} (Fig. 6b). The fabricated sensor provided a wide-ranging response and favorable sensitivity, enabling it for use in the detection of APX in unprocessed human plasma samples.

The analytical features of the developed method were compared with those of the previously reported method and are collected in Table 1. It is concluded that the fabricated probe is able to determine APX concentrations in a wide range, and also this probe can detect APX in plasma samples without any need for the pretreatment steps. Usually, separation-based and optical methods require a protein precipitation step to remove interfering biomolecules, resulting in the washing out of the analyte. This type of analytical probe is advantageous in clinical use, especially when a large number of plasma samples should be determined in a short period.[45–47]

3.6. Method validation

3.6.1. Repeatability, accuracy, and reproducibility. The intraday and interday precision of the fabricated probe was determined by selecting three concentrations of APX from the linear dynamic range. The obtained data points are collected in Table 2. The probe's precision was calculated as relative standard deviation (RSD%), calculated by dividing the standard deviation (SD) by the average and multiplying it by 100. The probe accuracy was also measured in the selected concentration, expressed as relative error percentage (RE%). RE% is calculated by multiplying the difference between the actual and calculated values by 100 and dividing it by the actual value. The calculated mean absolute RSD% and RE% confirmed that the probe has acceptable precision and accuracy, with 9.2% and 10.98%, respectively. It is noteworthy that the Food and Drug Administration (FDA) allows RSD% and RE% variations between +15% and −15% for all concentrations except LLOQs (±20%).

Reproducibility is another form of precision, which refers to the consistency of measurement results obtained in different laboratories. Reproducibility is not always necessary for validating methods in a single laboratory; it can be useful when standardizing analytical methods or using them across multiple labs. To test, two concentrations from the dynamic range, *i.e.*, 1.0 and 2.5 µg mL^{-1} were selected and determined by the developed approach. The obtained data approved the reproducibility of the probe with 13.1% and 11.8% for 1.0 and 2.5 µg mL^{-1}, respectively.

3.6.2. Specificity of the probe. Specificity means how a probe can detect the analyte concentration in the presence of coexisting agents with high accuracy. The specificity of the BFO/EEGO AG modified GCE was measured in the presence of some biologically available agents. The selected agents could be categorized in three different groups of biomolecules, ions, and pharmaceuticals (Fig. S3†). The probe signal was measured in the presence and absence of the agents and the interfering effect was calculated and reported as relative error (RE%). The obtained interfering test results confirmed the selective function of the fabricated probe toward the quantification of APX. Although a protein precipitation-free approach was utilized in the fabrication and detection process, the obtained specificity results are favorable. This performance may be produced by the used materials in the modification of the GCE. There are some reports that explored the antifouling effect of carbon-based materials by physical filtering ability.[44]

3.6.3. Stability tests. There are different stability tests in the fabrication of a sensing probe including analyte stability, and probe stability. The stability of the analyte could be checked by freeze-thaw, bench top, and stock solution stability tests. In the freeze-thaw stability test, the stability of the analyte during various freeze-thaw cycles is measured with measuring the concentration of three levels of APX in plasma samples after three freeze–thaw cycles. The bench-top stability test measures the amount of the analyte 6–12 h after leaving the plasma samples on the bench of the laboratory. Also, stock solution stability measures the stability of prepared stocks for the

Table 2 Accuracy and precision of the developed BFO/EEGO-AG method for APX detection in unprocessed plasma samples

Nominal concentration (µg mL^{-1})	Intraday precision (RSD%)	Interday precision (RSD%)	Intraday accuracy (RE%)	Interday accuracy (RE%)
0.3	9.3	10.0	8.1	13.0
2.5	10.7	11.5	9.2	14.0
5.0	10.9	−2.5	−10.1	−11.5

Table 3 Stock solution and freeze–thaw stability of the APX

	Stock solution		Freeze–thaw	
Concentration (μg mL^{-1})	Mean found (μg mL^{-1})	Accuracy (RE%)	Mean found (μg mL^{-1})	Accuracy (RE%)
0.3	0.29	3.3	0.23	10.0
2.5	2.23	10.8	2.26	9.6

Table 4 Determination of APX concentrations in patient plasma samples

Sample No.	Sexuality	Age (year)	Prescribed dose (mg)	Consumption in 24 h	Detected concentration (mg L^{-1})
1	Male	76	2.5	4	1.34
2	Male	58	2.5	2	1.11
3	Female	78	5.0	2	0.66
4	Male	81	2.5	2	0.49
5	Female	70	5.0	2	0.11

standard analyte at room temperature and in a refrigerator. All of the stability test results are expressed in RSD%. Table 3 lists the obtained stability results, in which the stability of APX is confirmed.[21]

The stability of the fabricated BFO/EEGO AG modified GCE probe was also investigated by plotting CVs at different cycle numbers. As shown in Fig. S4,† upon increasing the CV number, the peak current remained constant, proposing a stable response of the EEGO AG/BFO modified GCE during various CVs. However, the fabricated device could be utilized for only one test of real samples.

3.7. Applications of the sensor for detection of APX in patients' plasma samples

The BFO/EEGO AG modified GCE probe was employed to quantify APX levels in patients' plasma samples. To measure APX in patients' samples, about 0.25 mL of plasma samples was added to about 4.75 mL of Fe(CN)$_6^{4-}$/Fe(CN)$_6^{3-}$ solution (without any protein precipitation). The peak currents were recorded in the blank and patients' plasms by the DPV technique. The calibration curve equation was used to calculate the APX concentration. The obtained concentrations of APX in patients' plasma samples are presented in Table 4.

4. Conclusion

A novel electrochemical sensor was fabricated by layer-by-layer modification of the surface of a GCE with BFO and EEGO AG particles. The fabricated probe was used to determine APX in plasma samples. The signal of the electrode for APX was optimized to provide the highest oxidation current and also the accuracy and precision of the fabricated method were validated to assure reliable detection of APX. This probe showed a wide dynamic range from 10 ng mL^{-1} to 10 μg mL^{-1} with a low limit

of quantification (LLOQ) of 10 ng mL^{-1}. The BFO/EEGO AG modified GCE probe was employed for direct detection of APX in plasma samples without any need for pre-concentration and protein precipitation steps. Hence, the fabricated sensor has a promising potential for the quantification of trace concentrations of APX in unprocessed plasma samples.

Conflicts of interest

There are no conflicts to declare.

Acknowledgements

References

1 P. C. Wong, D. J. P. Pinto and D. Zhang, *J. Thromb. Thrombolysis*, 2011, **31**, 478–492.

2 S. Krishnaswamy, *J. Thromb. Haemostasis*, 2013, **11**(1), 265–276.

3 H. A. Hillarp, F. Baghei, I. Fagergerg Blixter, K. M. Gustafsson, L. Stigendal, M. Sten-Linder, K. Strandberg and T. L. Linahl, *J. Thromb. Haemostasis*, 2011, **9**, 133–139.

4 S. J. Wilson, T. M. Connolly, G. Peters, A. Ghosh, M. Johnson and D. E. Newby, *Cardiovasc. Res.*, 2019, **115**, 669–677.

5 S. J. Connolly, J. Eikelboom, C. Joyner, H.-C. Diener, R. Hart, S. Golitsyn, G. Flaker, A. Avezum, S. H. Hohnloser, R. Diaz, M. Talajic, J. Zhu, P. Pais, A. Budaj, A. Parkhomenko, P. Jansky, P. Commerford, R. S. Tan, K.-H. Sim, B. S. Lewis, W. Van Mieghem, G. Y. H. Lip, J. H. Kim, F. Lanas-Zanetti, A. Gonzalez-Hermosillo, A. L. Dans, M. Munawar, M. O'Donnell, J. Lawrence, G. Lewis, R. Afzal and S. Yusuf, *N. Engl. J. Med.*, 2011, **364**, 806–817.

6 L. Fauchier and N. Clementy, *N. Engl. J. Med.*, 2011, **365**, 1844–1845.

7 W. Byon, S. Garonzik, R. A. Boyd and C. E. Frost, *Clin. Pharmacokinet.*, 2019, **58**, 1265–1279.

8 Y.-K. Lee and M. R. Player, *Med. Res. Rev.*, 2011, **31**, 202–283.

9 H. Partsch, *Vasa*, 2009, **38**, 13–29.

10 F. Gouveia, J. Bicker, J. Santos, M. Rocha, G. Alves, A. Falcão and A. Fortuna, *J. Pharm. Biomed. Anal.*, 2020, **181**, 113109.

11 M. M. Samama and G. T. Gerotziafas, *J. Thromb. Thrombolysis*, 2010, **29**, 92–104.

12 J.-P. Bassand, *EP Eur.*, 2012, **14**, 312–324.

13 J. Stangier, *Clin. Pharmacokinet.*, 2008, **47**, 285–295.

14 J. Santos, N. António, M. Rocha and A. Fortuna, *Br. J. Clin. Pharmacol.*, 2020, **86**, 533–547.

15 J. M. Andreu Cayuelas, C. Caro Martínez, P. J. Flores Blanco, G. Elvira Ruiz, H. Albendin Iglesias, J. J. Cerezo Manchado, J. L. Bailen Lorenzo, J. L. Januzzi, A. García Alberola and S. Manzano-Fernández, *Eur. J. Clin. Invest.*, 2018, **48**, e12907.

16 L. F. Buckley, E. Rybak, A. Aldemerdash, J. W. M. Cheng and J. Fanikos, *Clin. Cardiol.*, 2017, **40**, 46–52.

17 M. M. Samama and C. Guinet, *Clin. Chem. Lab. Med.*, 2011, **49**, 761–772.

18 J. Albiol-Chiva, J. Peris-Vicente, D. García-Ferrer and J. Esteve-Romero, *J. Chromatogr. B: Anal. Technol. Biomed. Life Sci.*, 2019, **1120**, 8–15.

19 M. Szultka-Młyńska, S. Bajkacz, M. Kaca, I. Baranowska and B. Buszewski, *J. Chromatogr. B: Anal. Technol. Biomed. Life Sci.*, 2018, **1093–1094**, 100–112.

20 J. Lagoutte-Renosi, J. Le Poupon, A. Girard, D. Montange and S. Davani, *J. Chromatogr. B: Anal. Technol. Biomed. Life Sci.*, 2018, **1100–1101**, 43–49.

21 A. Jouyban, M. Shaghaghi, J. L. Manzoori, J. Soleymani and J. Vaez-Gharamaleki, *Iran. J. Pharm. Res.*, 2011, **10**, 695–704.

22 P. Shahbazi-Derakhshi, E. Mahmoudi, M. M. Majidi, H. Sohrabi, M. Amini, M. R. Majidi, A. Niaei, N. Shaykh-Baygloo and A. Mokhtarzadeh, *Biosensors*, 2023, 13.

23 H. Sohrabi, M. R. Majidi, O. Arbabzadeh, P. Khaaki, S. Pourmohammad, A. Khataee and Y. Orooji, *Environ. Res.*, 2022, **204**, 112082.

24 J. Soleymani, D. Perez-Guaita, M. Hasanzadeh, N. Shadjou and A. Jouyban, *TrAC, Trends Anal. Chem.*, 2017, **86**, 122–142.

25 J. Soleymani, M. Hasanzadeh, M. H. Somi and A. Jouyban, *Mater. Sci. Eng., C*, 2020, **107**, 110320.

26 H. Kholafazad Kordasht, M.-H. M.-H. Moosavy, M. Hasanzadeh, J. Soleymani and A. Mokhtarzadeh, *Anal. Methods*, 2019, **11**, 3910–3919.

27 V. Shafiei-Irannejad, J. Soleymani, S. Azizi, M. KhoubnasabJafari, A. Jouyban and M. Hasanzadeh, *TrAC, Trends Anal. Chem.*, 2019, **116**, 1–12.

28 J. Soleymani, M. Hasanzadeh, M. Eskandani, M. Khoubnasabjafari, N. Shadjou and A. Jouyban, *Mater. Sci. Eng., C*, 2017, **77**, 790–802.

29 A. Saenchoopa, W. Boonta, C. Talodthaisong, O. Srichaiyapol, R. Patramanon and S. Kulchat, *Spectrochim. Acta, Part A*, 2021, **251**, 119433.

30 W. Zhao, H. Zhang, J. Liu, L. Xu, H. Wu, M. Zou, Q. Wang, X. He, Y. Li and A. Cao, *Small*, 2018, **14**, 1802394.

31 H. Maleki, *Chem. Eng. J.*, 2016, **300**, 98–118.

32 B. Khalilzadeh, N. Shadjou, H. N. Charoudeh and M.-R. Rashidi, *Microchim. Acta*, 2017, **184**, 3651–3662.

33 R. Pourakbari, N. Shadjou, H. Yousefi, I. Isildak, M. Yousefi, M.-R. Rashidi and B. Khalilzadeh, *Microchim. Acta*, 2019, **186**, 820.

34 H. Nasrollahpour, M. Mahdipour, I. Isildak, M.-R. Rashidi, A. Naseri and B. Khalilzadeh, *Biosens. Bioelectron.*, 2021, **178**, 113023.

35 M. Moradi, J. Soleymani and A. Jouyban, *J. Pharm. Biomed. Anal.*, 2022, **214**, 114746.

36 C.-H. Chen, S. Hu, J.-F. Shih, C.-Y. Yang, Y.-W. Luo, R.-H. Jhang, C.-M. Chiang and Y.-J. Hung, *Sci. Rep.*, 2017, **7**, 3908.

37 L. Ruiyi, W. Jiajia, L. Ling and L. Zaijun, *Microchim. Acta*, 2016, **183**, 1641–1649.

38 K. Wang, X. Xu, L. Lu, H. Wang, Y. Li, Y. Wu, J. Miao, J. Z. Zhang and Y. Jiang, *ACS Appl. Mater. Interfaces*, 2018, **10**, 12698–12707.

39 X. Mi, G. Huang, W. Xie, W. Wang, Y. Liu and J. Gao, *Carbon*, 2012, **50**, 4856–4864.

40 J. Soleymani, F. Feyzi, S. Dastmalchi, F. Ranjbar and A. Jouyban, *J. Sep. Sci.*, 2023, 2201028.

41 G. Gorgolis and C. Galiotis, *2D Mater.*, 2017, **4**, 32001.

42 H. Zhang, T. Tong, J. Chen and J. Cheng, *J. Sol-Gel Sci. Technol.*, 2016, **78**, 135–143.

43 A. J. Bard and L. R. Faulkner, in *Electrochemical Methods*, Wiley, New York, 2nd edn, 2001, pp. 580–632.

44 M. Mahmoudpour, A. Jouyban, J. Soleymani and M. Rahimi, *Adv. Colloid Interface Sci.*, 2022, **302**, 102637.

45 J. Soleymani, D. Perez-Guaita, M. Hasanzadeh, N. Shadjou and A. Jouyban, *TrAC, Trends Anal. Chem.*, 2017, **86**, 122–142.

46 J. Soleymani, M. Hasanzadeh, M. Eskandani, M. Khoubnasabjafari, N. Shadjou and A. Jouyban, *Mater. Sci. Eng., C*, 2017, **77**, 790–802.

47 J. Soleymani, M. Hasanzadeh, N. Shadjou, M. H. Somi and A. Jouyban, *J. Pharm. Biomed. Anal.*, 2020, **180**, 113077.

48 X. Delavenne, P. Mismetti and T. Basset, *J. Pharm. Biomed. Anal.*, 2013, **78**, 150–153.

49 W. Zhang, D. Lou, D. Zhang, Y. Zhang and H. Huang, *J. Thromb. Thrombolysis*, 2016, **42**, 205–211.

50 M. Rizk, M. A. Sultan, E. A. Taha, A. K. Attia and Y. M. Abdallah, *Anal. Methods*, 2017, **9**, 2523–2534.

51 M. Cini, C. Legnani, R. Padrini, B. Cosmi, C. Dellanoce, G. De Rosa, R. Marcucci, V. Pengo, D. Poli, S. Testa and G. Palareti, *Int. J. Lab. Hematol.*, 2020, **42**, 214–222.

52 H. K. Jain and V. K. Nikam, *Int. J. Pharm. Pharm. Sci.*, 2017, **9**, 24–32.

53 S. S. Prabhune, R. S. Jaguste, P. L. Kondalkar and N. S. Pradhan, *Sci. Pharm.*, 2014, **82**, 777–786.

54 R. I. El-Bagary, E. F. Elkady, N. A. Farid and N. F. Youssef, *Spectrochim. Acta, Part A*, 2017, **174**, 326–330.

55 S. Lessire, A. Dincq, R. Siriez, L. Pochet, A. Sennesael, O. Vornicu, M. Hardy, O. Deceuninck, J. Douxfils and F. Mullier, *Int. J. Lab. Hematol.*, 2020, **42**, 394–402.

© 2023 The Author(s). Published by the Royal Society of Chemistry